

*Supporting Information for*

## **Enthalpic and Entropic Contributions to Fast Lithium Ion Conduction in Solid-State Aqueous Polymer Electrolytes**

*Jae Hyun Park<sup>1),\*</sup>, Sungyeob Jung<sup>2)</sup>, Puji Lestari Handayani<sup>3)</sup>, Narayana Aluru<sup>4)</sup>, Taehoon Kim<sup>5)</sup>,  
Sang Bok Lee<sup>5)</sup>, U Hyeok Choi<sup>3)</sup>,\*\*, and Jaekwang Lee<sup>2)</sup>,\*\*\**

<sup>1)</sup> Department of Aerospace and Software Engineering, Gyeongsang National University, Jinju, Gyeongnam 52828, South Korea

<sup>2)</sup> Department of Physics, Pusan National University, Busan 46241, South Korea

<sup>3)</sup> Department of Polymer Science and Engineering and Program in Environmental and Polymer Engineering, Inha University, Incheon 22212, South Korea

<sup>4)</sup> Oden Institute, Department of Mechanical Engineering, The University of Texas at Austin, Austin, TX 78712, U.S.A.

<sup>5)</sup> Composites Research Division, Korea Institute of Materials Science, Changwon, Gyeongnam 51508, South Korea

\*corresponding author. E-mail: [parkj@gnu.ac.kr](mailto:parkj@gnu.ac.kr)

\*\*corresponding author. E-mail: [uhyeok@inha.ac.kr](mailto:uhyeok@inha.ac.kr)

\*\*\*corresponding author. E-mail: [jaekwangl@pusan.ac.kr](mailto:jaekwangl@pusan.ac.kr)

## Table of Contents

S1. Movie file .....	S2
S2. Preparation of SAPE .....	S3
S3. Structure and Properties of SAPE .....	S5
S4. Electrochemical Performance of SAPE .....	S7
S5. Dominance of Li <sup>+</sup> -ion Transport in the Conductivity of SAPE .....	S9
S6. Molecular Dynamics Simulations .....	S10
S7. Distribution of Li-Li Distance .....	S11
S8. Polymer Aggregations at Different Temperatures .....	S12
S9. Pore-Size Distributions (PSDs) under Fixed Water Content Condition .....	S15
S10. Energy Barrier for Ionic Conductivity in SAPE .....	S16
S11. References .....	S18

## S1. Movies File

In the movie file (ion movement visualization.mp4), three animations are presented: (left)  $T = 280$  K,  $\phi_{\text{wt}} = 0.6$ ; (middle)  $T = 300$  K,  $\phi_{\text{wt}} = 0.7$ ; (right)  $T = 320$  K,  $\phi_{\text{wt}} = 0.8$ . The dimension of simulation box varies depending on  $T$  and  $\phi_{\text{wt}}$  according to the number of water molecules.

## S2. Preparation of SAPE

\*[R1], [R2], ...: References. List of references are given at the end of supporting information.

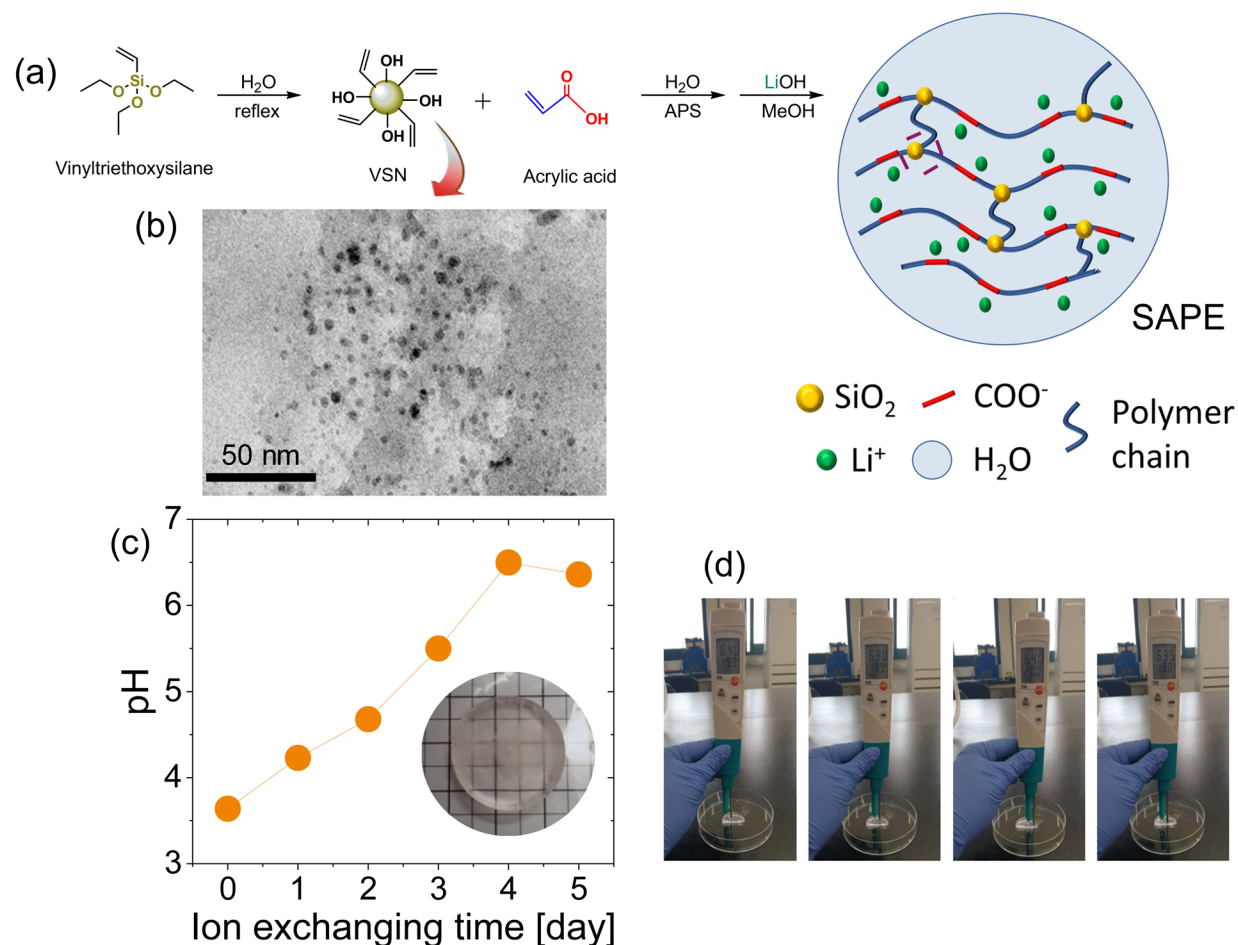


**Figure S1.** (a) Preparation of solid-state aqueous polymer electrolytes (SAPE) using vinyl silica nanoparticles (VSNs) as cross-linkers and acrylic acid monomers via sol-gel reaction and free radical polymerization [R1]\*. (b) Transmission electron microscope (TEM) image of VSNs with an average diameter of 5 nm. (c) pH versus Ion exchanging time of SAPE containing  $Li^+$  counteranions and SAPE photograph in the inset [R1]. (d) Photographs of measuring pH of four different points in SAPE after ion exchanging process, showing the average pH of 6.36, which is close to that of water [R1].

PAA-based solid-state aqueous polymer electrolytes (SAPes) were prepared through two-step processes of sol-gel reaction and free radical polymerization (**Figure S1a**). The sol-gel reaction

was used to prepare vinyl silica nanoparticles (VSN with an average diameter of 5 nm shown in **Figure S1b**) that serve as strong cross-linkers to create a solid-state network structure. The radical polymerization of acrylic acid monomers was done with ammonium persulfate (APS) as an initiator in the VSN dispersed aqueous solution. To neutralize the prepared hydrogel with  $\text{Li}^+$  cations, ion exchange from the  $\text{H}^+$  to  $\text{Li}^+$  was done in MeOH with excess LiOH. The amount of the silica nanoparticles (VSN) in SAPE was 0.8 wt%, along with PAA (16.8 wt%) and  $\text{H}_2\text{O}$  (82.4 wt%). The detailed preparations of the SAPE with highly diluted nanoparticles were described in an earlier study [R1]. To investigate the  $\text{Li}^+$  neutralization level, the pH of SAPE was explored as a function of ion exchanging time (**Figure S1c**). Before the ion exchanging procedure, the membrane exhibited pH  $\sim 3.4$ . The pH value increased with the ion exchanging time, and eventually approached to pH  $\sim 6.36$  (**Figure S1d**), which is within the normal range for pH in water. After conducting the pH value analysis, the extent of  $\text{Li}^+$  neutralization level was 99% neutralized with  $\text{Li}^+$ . This was confirmed by elemental analysis from inductively coupled plasma mass spectrometry (Perkinelmer ELAN6100).

### S3. Structure and Properties of SAPE

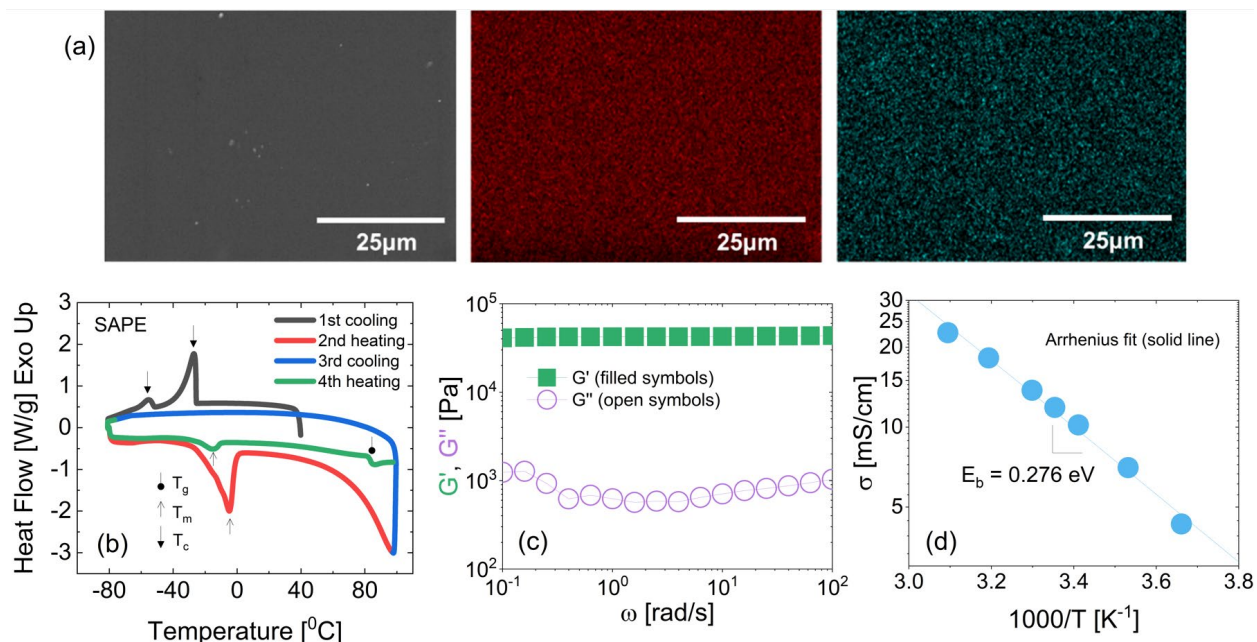


**Figure S2.** (a) Cross-sectional FE-SEM image (left) of SAPE after extracting water from SAPE and its energy dispersive X-ray spectroscopy (EDS) elemental mapping of carbon (C, center) and silicon (Si, right) [R1]. (b) DSC thermograms of SAPE, where SAPE  $T_c$ ,  $T_m$ , and  $T_g$  were indicated by arrows [R1]. (c) Rheological measurements of SAPE showing storage modulus ( $G'$ , filled symbols, left axis), loss modulus ( $G''$ , open symbols, left axis), and tan delta ( $\tan\delta$ , X center symbol, right axis) versus angular frequency at room temperature. (d) Temperature dependence of ionic conductivity  $\sigma$  of SAPE with the activation energy of  $E_b = 0.276$  eV obtained from the Arrhenius equation fit to data (solid line).

The macroscopic morphology of SAPE was investigated using field emission-scanning electron microscopy (FE-SEM, JSM-6700F) with an accelerating voltage of 15.0 kV, after Pt sputter coating for 30 min, along with energy dispersive X-ray spectroscopy (EDS) mapping (**Figure S2a**). To clearly observe SAPE morphology, before FE-SEM analysis, the sample was freeze-dried for 2 days to extract water from the material. **Figure S2a** shows that the carbon and silicon signals were detected uniformly over the whole cross-section, indicating that the silica nanoparticles were evenly distributed within the PAA matrix. The measurement of the SAPE thermal properties (such as crystallization ( $T_c$ ), melting transition ( $T_m$ ), and glass transition ( $T_g$ ) temperatures) was

conducted using a TA Instrument Q2000 differential scanning calorimeter (DSC) with 10 K/min heating and cooling rates under an inert atmosphere. **Figure S2b** shows the DSC thermal curves of SAPE from four cycles. As expected, the first cooling and second heating scans reveal crystallization ( $T_c$ ) and melting transition ( $T_m$ ) temperatures due to the phase transition of water. However, at the third cooling cycle, there was no clear exotherm ( $T_c$ ), indicating that most of water may be evaporated during the second heating cycle. At the last heating scan, the residual water crystalized during the previous cooling cycle may produce the small endotherm ( $T_m$ ), and finally the glass transition temperature was observed at  $\sim 85^\circ\text{C}$ , which is close to that of pure PAA [R2]. In order to investigate the mechanical properties of SAPE, rheological measurements were performed using oscillatory shear. **Figure S2c** shows the storage modulus ( $G'$ , filled symbols), loss modulus ( $G''$ , open symbols), and tan delta ( $\tan\delta$ , X center symbols) as a function of frequency for SAPE. Its  $G' > G''$  and  $\tan\delta < 0$  over the range of frequencies, indicating that this SAPE follows solid behavior. Furthermore, the  $G'$  and  $G''$  are relatively independent of frequency, which is the typical characteristic of a cross-linked gel having a network structure. The shear modulus ( $G' = 42.3 \text{ kPa}$  at  $T = 298 \text{ K}$ ) observed in SAPE corresponds to the gel modulus ( $G' = G_e = \nu kT = \rho RT/M_x$ , where  $\nu = \rho N_A/M_x$  is the number density of network strands,  $\rho = 1.544 \text{ g/cm}^3$  is the polymer density,  $N_A$  is the Avogadro's number,  $k$  is the Boltzmann constant,  $R = N_A k$  is the gas constant, and  $M_x$  is the molecular weight of a network strand) [R3]. This allows us to calculate the molecular weight of the PAA network strand ( $M_x \sim 90,100 \text{ g/mol}$ ) and the average length of the PAA chain between VSNs ( $N_x = M_x/M_0 = 1250$ , where  $M_0$  is the molecular weight of acrylic acid (AA) monomer). These values are similar to those of PAA without silica cross-linkers [R2]. **Figure S2d** displays the temperature dependence of SAPE ionic conductivity  $\sigma$ , measured by Novocontrol GmbH Concept 40 broadband dielectric relaxation spectrometer and Quatro Cryosystem sample chamber containing a vacuum-isolated cryostat and nitrogen line using a sinusoidal voltage with an amplitude of 0.1 V. The  $\sigma(T)$  temperature dependence is well described by the Arrhenius equation ( $\sigma = A_\sigma/T \exp(-E_b/RT)$ , where  $A_\sigma$  is the pre-exponential factor and  $E_b$  is the total energy barrier for ion conduction). The solid line in **Figure S2d** is a fit to the Arrhenius equation, and the obtained energy barrier is  $E_b = 0.276 \text{ eV}$ .

## S4. Electrochemical Performance of SAPE

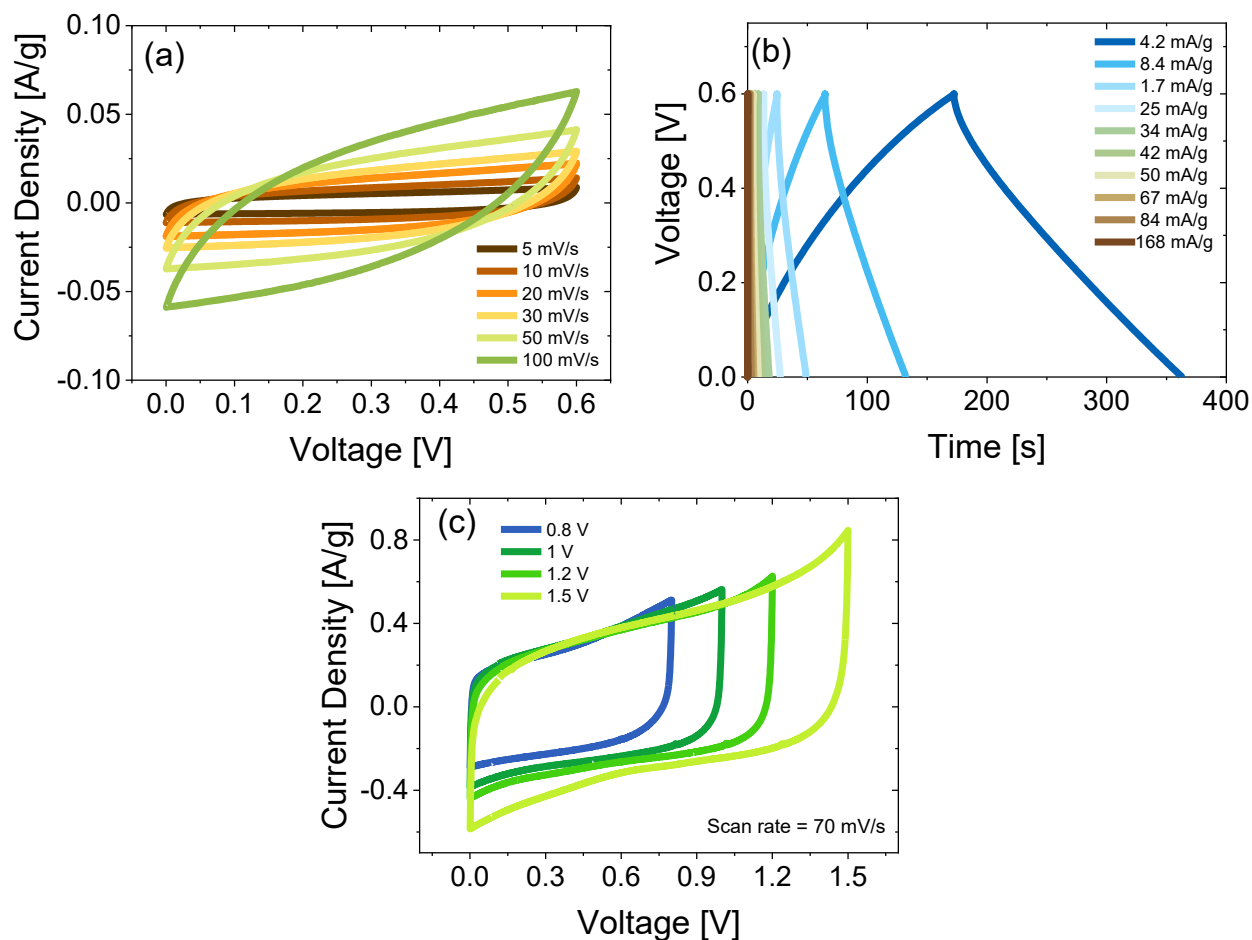


**Figure S3.** Electrochemical properties of solid-state supercapacitors, assembled with the PAA-based SAPE and two carbon nanotube yarn (CNTY) electrodes (CNTY/SAPE/CNTY); (a) voltage dependence of current density (CV profiles) at different scan rates from 5 to 100 mV/s under 0.6 V voltage window, (b) galvanostatic charge-discharge (GCD profiles) at different current densities from 4.2 to 168 mA/g, and (c) CV profiles at a scan rate of 70 mV/s in different voltage windows (0.8, 1, 1.2, and 1.5 V).

To verify the electrochemical stability of our PAA-based SAPE, we performed the electrochemical measurements in the two-electrode configuration; i.e., symmetric supercapacitor cells, where the SAPE was sandwiched between carbon nanotube yarn (CNTY) electrodes



(CNTY/SAPE/CNTY) (Na *et al.*, 2022). **Figure S3a** displays the scan rate (5 – 100 mV/s) dependent cyclic voltammetry (CV) curves of the CNTY/SAPE/CNTY device, indicating the electrical double layer (EDL) supercapacitor with a stable and symmetric shape under 0 – 0.6 V voltage window, even for a high scan rate of the CV curve. In addition, the galvanostatic charge-discharge (GCD) tests were performed at various current densities (4.2 – 168 mA/g) to evaluate the capacitive behavior of the CNTY/SAPE/CNTY supercapacitor (**Figure S3b**). The linear potential-time relation indicates the stable performance of the supercapacitor during the charge-discharge cycle under 0 – 0.6 V, consistent with the observation from the CV measurements. This suggests that the PAA-based SAPE could work well as an electrolyte for energy storage devices. The electrochemical stability window of the SAPE was further investigated in different voltage windows (**Figure S3c**). In **Figure S3c**, the stable operating electrochemical voltage window of the supercapacitor (CNTY/SAPE/CNTY) could be expanded from 0.8, 1.0, 1.2 to 1.5 V. Consequently, such a stable electrochemical performance up to 1.5 V demonstrates the possibility of using this SAPE even in voltage windows above 1.0 V.

## S5. Dominance of Li<sup>+</sup>-ion Transport in the Conductivity of SAPE

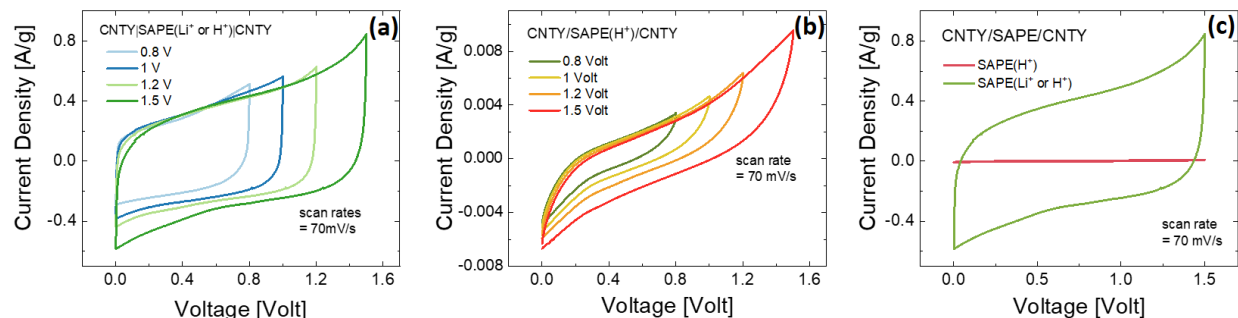


**Figure S4.** (a-c) Electrochemical properties (CV curves) of solid-state supercapacitors, assembled with either SAPE with Li<sup>+</sup>-ion exchange or SAPE without Li<sup>+</sup>-ion exchange and two carbon nanotube yarn (CNTY) electrodes (CNTY/SAPE(Li<sup>+</sup> or H<sup>+</sup>)/CNTY and CNTY/SAPE(H<sup>+</sup>)/CNTY, respectively); CV profiles at a scan rate of 70 mV/s in different voltage windows (0.8, 1, 1.2, and 1.5 V) for (a) CNTY/SAPE(Li<sup>+</sup> or H<sup>+</sup>)/CNTY and (b) CNTY/SAPE(H<sup>+</sup>)/CNTY and (c) their CV comparison at 1.5 V.

To verify the dominance of Li<sup>+</sup>-ion transport in the conductivity of the present PAA-based SAPE, we additionally performed the electrochemical measurements in the symmetric supercapacitor cells with two different electrolytes; i.e., SAPE with the Li<sup>+</sup>-ion exchanging process (see **Figure S4a**) and SAPE without the Li<sup>+</sup>-ion exchanging process (see **Figure S4b**). Hence, the electrolyte [SAPE(H<sup>+</sup> or Li<sup>+</sup>)] in **Figure S4a** has two possible charge carriers (H<sup>+</sup> or Li<sup>+</sup>), whereas the electrolyte [SAPE(H<sup>+</sup>)] in **Figure S4b** only has one type of charge carrier (H<sup>+</sup>). Both the SAPEs were sandwiched between two carbon nanotube yarn (CNTY) electrodes and their electrochemical performance was investigated using cyclic voltammetry (CV) measurements. In both the SAPEs, the stable operating electrochemical voltage window of the supercapacitor (CNTY/SAPE/CNTY) could be expanded from 0.8, 1.0, 1.2 to 1.5 V (Figures R1a and R1b). However, when directly comparing their CV curves at 1.5 V between SAPE (H<sup>+</sup> or Li<sup>+</sup>) and SAPE(H<sup>+</sup>), the SAPE containing the Li<sup>+</sup> charge carriers shows a much higher current density than the SAPE containing the only H<sup>+</sup> charge carriers (see **Figure S4c**). This indicates that most of the capacitance observed in the supercapacitor is due to the Li<sup>+</sup> transport and the H<sup>+</sup> contribution is relatively small.

## S6. Molecular Dynamics Simulations

In this study, PAA was modeled with a united atom model, and the atomic charges and Lennard-Jones (LJ) parameters were taken from the values in GROMOS force field [R7]. The waters were modelled with SPC/E model [R8]. The LJ parameters for  $\text{Li}^+$  were taken from the Dang parameter [R9, R10, R11]. All the MD simulations were performed with GROMACS 4.6.7 [R7]. For the MD simulations, initially PAA molecules,  $\text{Li}^+$ , and water molecules were put together in a sufficiently large simulation box according to the given water content at a high temperature of  $T = 1000$  K. Then, an annealing process was applied to obtain an equilibrium system at pressure of  $p = 1.0$  atm and an assigned temperature. At the end of the process, the system was equilibrated with NPT ensemble for 5.0 ns. The system temperature and pressure were regulated with Nosé-Hoover thermostat [R12, R13] and Parrinello-Rahman barostat [R14, R15], respectively. Finally, the simulation was proceeded for 40 to 90 ns more to produce the data. The timestep for the simulations was 1.0 fs.

## S7. Distribution of Li-Li Distance

In the present system, the mobile anions are not included and hence the conventional ion pairings do not exist. Instead, the positive Li-ions are attracted to the negative oxygen atoms in the immobile PAAs. However, as revealed in **Figure S5**, 95 % of the Li-Li pair has a distance larger than 2.0 nm regardless of the condition. In that range of distance, direct electrostatic and van der Waals interactions become considerably reduced, and we can state that a collective motion of Li-ions does not appear. It confirms the feasibility of the Nernst-Einstein relation assuming a dilute limit for the present systems.

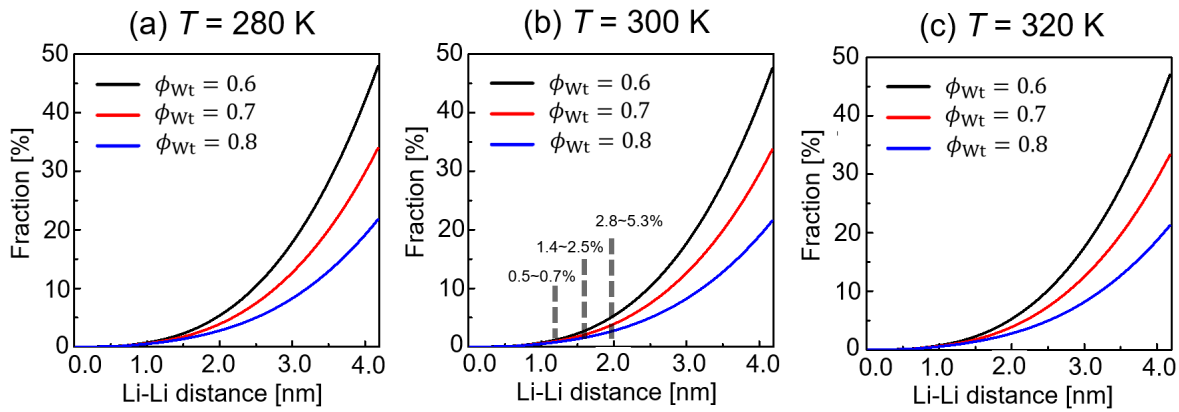


**Figure S5.** Distribution of Li-Li distance at  $T = 280$  K, 300 K, and 320 K.

## S8. Polymer Aggregations at Different Temperatures

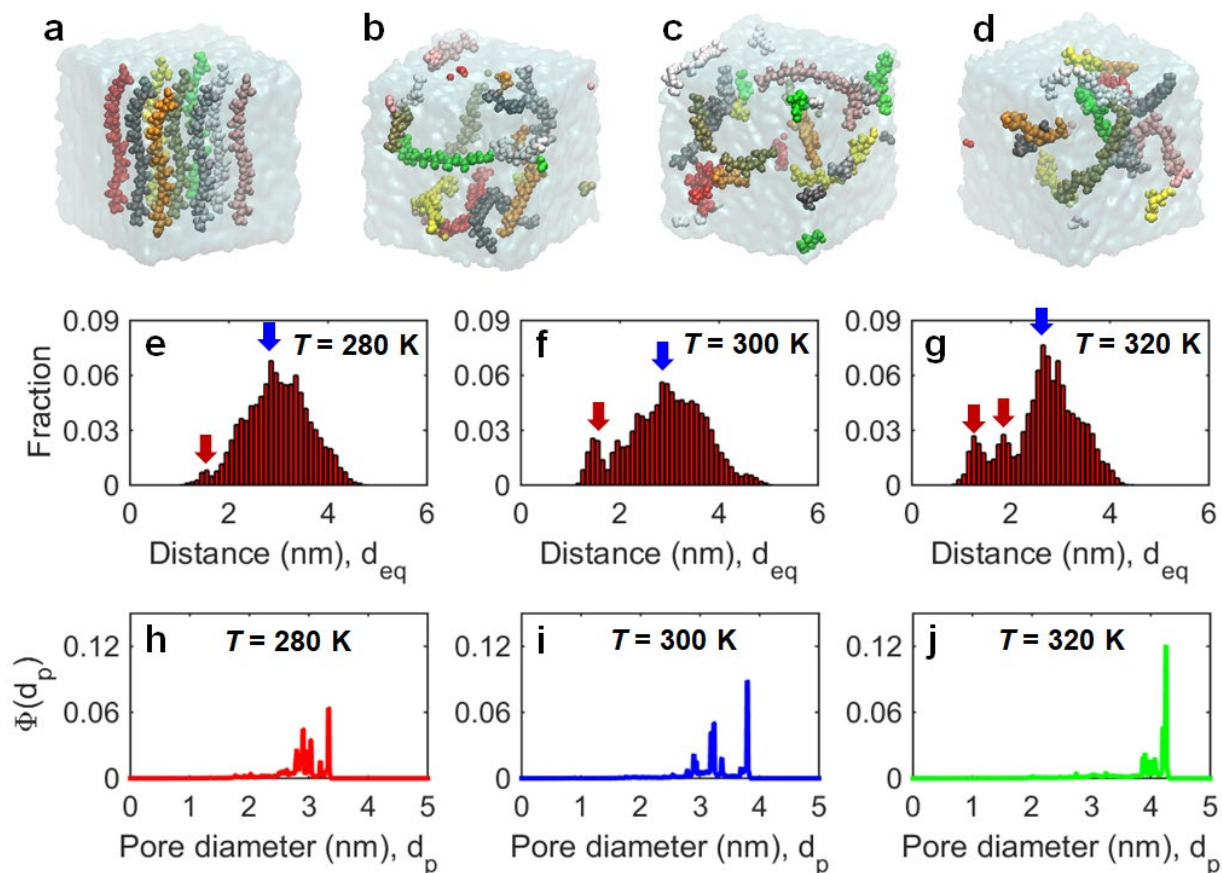


**Figure S6.** MD simulations for polymer aggregation: (a) Initial configuration. Each polymer chain is distinguished by a different color. The lithium ions are not shown while the water box is expressed as transparent sky blue; (b-d) Equilibrated configuration: (b) at  $T = 280$  K, (c) at  $T = 300$  K, and (d) at  $T = 320$  K; (e-g) Distribution of the equilibrium center-to-center distance between polymer chains: (e) at  $T = 280$  K, (f) at  $T = 300$  K, and (g) at  $T = 320$  K. The water molecules and lithium ions are not shown; (h-j) Pore size distributions (PSDs),  $\Phi(d_p)$ : (h) at  $T = 280$  K, (i)  $T = 300$  K, and (j)  $T = 320$  K.

We performed additional MD simulations to examine how the group-behavior of polymers is altered with temperature. For this purpose, we considered a water box of  $6 \times 6 \times 6$  nm<sup>3</sup>, which contained nine PAA chains with 20 monomers each (see **Figure S6a**). The chains were placed in a parallel arrangement with equal spacing. The length of a single PAA chain was about 5.1 nm. A

number of Li-ions appropriate to neutralize the system were added. Then, this system was equilibrated under periodic boundary conditions for 45 ns with the NPT ensemble at three different temperatures ( $T = 280, 300$ , and  $320$  K). The pressure was fixed at  $p = 1.0$  atm for all the simulations. The conformations of polymer chains equilibrated at  $T = 280, 300$ , and  $320$  K are visualized in **Figures S6b, S6c, and S6d**, respectively. The PAA chains aggregated more closely at higher temperatures, which was confirmed quantitatively by investigating the distribution of the center-to-center distance between polymers at equilibrium,  $d_{eq}$  (see **Figures S6e, S6f, and S6g**). In the figures, the major distribution indicated by a blue arrow (near  $d_{eq} = 3$  nm) presents the equilibrium distances formed by the weak interactions between polymers, while the minor peaks marked with a red arrow originate from a closer aggregation of a specific polymer pair. With the increase in  $T$ , the minor peaks in the region of small  $d_{eq}$  began growing. Notably, there is only one small peak at  $T = 300$  K, but two small peaks are observed at  $T = 320$  K. The mean of  $d_{eq}$ -distribution,  $\bar{d}_{eq}$ , is reduced as  $T$  increases:  $\bar{d}_{eq} = 3.35 \pm 0.78$  nm at  $T = 280$  K;  $\bar{d}_{eq} = 3.29 \pm 0.91$  nm at  $T = 300$  K; and  $\bar{d}_{eq} = 3.00 \pm 0.83$  nm at  $T = 320$  K. As the temperature rises, the hydrogen bonds from the surroundings (water) to the polymer weakens and the polymers become more mobile so that negative PAA chains are easily aggregated through the mediation of positive lithium ions. The enhanced aggregation leads to *phase separation* between water and polymer [R16] as the water-occupying space (i.e., *water tubes* in an electrolyte) grows bigger.

For the further quantitative analysis of the polymer aggregations, we computed the pore size distribution (PSD) using the Zeo++ package [R17, R18]. Throughout this letter, the pore indicates a water tube. **Figures S6h, S6i, and S6j** present the PSDs at  $T = 280, 300$ , and  $320$  K, respectively. In constructing PSDs, we first removed the water and ions from an equilibrated MD configuration to generate polymer chains and voids only. Then, we used 50,000 Monte Carlo sampling with a probe of radius  $1.2$  Å to compute PSD in which the histogram bin size was  $0.1$  Å. In the PSDs, the biggest pore stands for the ambient space surrounding polymer aggregates while the small pores correspond to the accessible voids between polymers. At  $T = 320$  K, the peak corresponding to the biggest pore ( $d_p \approx 4.3$  nm) is much larger than the others. It means that most chains are aggregated to generate a large void separated from the aggregates. The minor peaks near  $d_p = 4.0$  nm are the tail of the biggest peak. At the middle temperature of  $T = 300$  K, the size of the biggest pore is

reduced to  $d_p \approx 3.8$  nm whereas the number of minor peaks with meaningful magnitude increases. Different from the system at  $T = 320$  K, in the system at  $T = 300$  K, the local voids between polymers and polymer groups become apparent, and as a result, the small peaks appear clearly. When the temperature is low ( $T = 280$  K), the polymer chains are distributed evenly and the size of the biggest pore ( $d_p \approx 3.3$  nm) is not much different from those of smaller ones ( $d_p = 2.8$  to  $3.0$  nm).

## S9. Pore-Size Distributions (PDSs) Under Fixed Water Content Condition

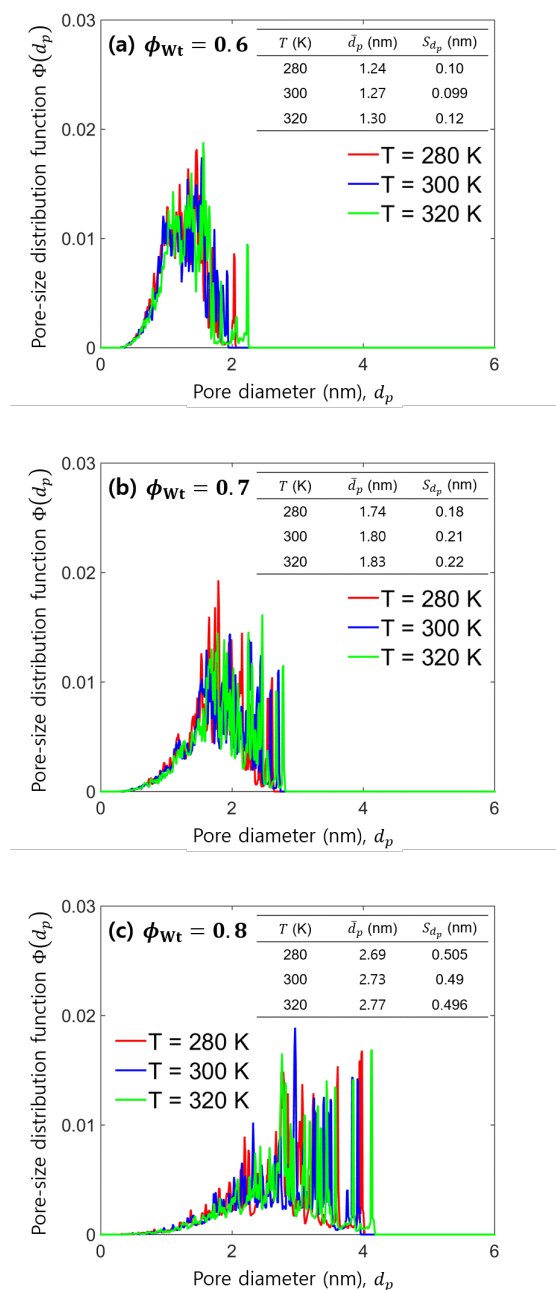


**Figure S7.** Comparison of PDS histograms at different temperatures ( $T = 280$  K, 300 K, and 320 K) for a given water content ( $\phi_{wt} = 0.6, 0.7$ , and 0.8).



## S10. Energy Barrier for Ionic Conductivity in SAPE

Consider the Nernst-Planck relation for ionic conductivity,

$$\sigma = \frac{n_{\text{Li}} e^2 D_{\text{Li}}}{k_B T}, \quad (\text{S1})$$

where  $n_{\text{Li}}$  is the ion number density and  $D_{\text{Li}}$  is the diffusion coefficient. Also, the diffusion coefficient can be expressed as:

$$D_{\text{Li}} = D_0 \exp\left(-\frac{\Delta G}{RT}\right), \quad (\text{S2})$$

where  $D_0$  is a coefficient,  $R$  is universal gas constant, and  $\Delta G$  is a free energy barrier across available hopping sites. The free energy barrier  $\Delta G$  is the sum of the enthalpic contribution,  $H$ , and the entropic contribution,  $-T\Delta S$ :

$$\Delta G = \Delta H - T\Delta S. \quad (\text{S3})$$

Here,  $\Delta H$  is enthalpy barrier and  $\Delta S$  is entropy of system. In the main text, equation (S3) is expressed in an alternative form:

$$E_b = E_H + E_S. \quad (\text{S4})$$

where  $E_b$  is energy barrier,  $E_H$  is enthalpic barrier, and  $E_S$  is entropic barrier to emphasize the physical understanding of conductivity.  $\Delta H$  is often referred to as *activation energy*,  $E_a$ , in the ionic conduction through solid electrolytes [R19, R20]. In solid electrolytes, the entropy does not vary significantly, so the entropic barrier is not considerable. Hence, the energy barrier is mainly determined from the enthalpic barrier, and the enthalpic barrier is often regarded as *activation energy* [R21, R22]. However, in this study, the enthalpic and entropic barriers should be distinguished since both the enthalpy and entropy determine the  $\text{Li}^+$  ion transport in SAPE.

From equations (S1), (S2), and (S3), the ionic conductivity can be rewritten as:

$$\sigma = \frac{e^2 D_0}{k_B} \cdot \frac{1}{T} \cdot n_{\text{Li}} \cdot \exp\left(\frac{\Delta S}{R}\right) \cdot \exp\left(-\frac{\Delta H}{RT}\right). \quad (\text{S5})$$

Considering  $n_{\text{Li}}$  and  $\Delta S$  are function of water content,  $\phi_{\text{wt}}$ :  $n_{\text{Li}} = n_{\text{Li}}(\phi_{\text{wt}})$  and  $\Delta S = \Delta S(\phi_{\text{wt}})$ , equation (S5) is simplified as:

$$\sigma = A \cdot \frac{1}{T} \cdot B(\phi_{Wt}) \cdot \exp\left(-\frac{\Delta H}{RT}\right), \quad (\text{S6})$$

where  $A = e^2 D_0 / k_B$  is a constant and

$$B(\phi_{Wt}) = n_{\text{Li}}(\phi_{Wt}) \cdot \exp\left(\frac{\Delta S(\phi_{Wt})}{R}\right). \quad (\text{S7})$$

### **S10.1. $\phi_{Wt} \neq \phi_{Wt}(T)$ : $\phi_{Wt}$ is not a function of temperature**

If  $\phi_{Wt}$  is not a function of temperature:  $\phi_{Wt} \neq \phi_{Wt}(T)$ ,  $B(\phi_{Wt})$  in equation (S6) is reduced to be a constant. Thus, the enthalpic barrier,  $\Delta H$ , becomes equivalent to the energy barrier of system,  $E_b$ , which is often expressed as,  $E_a$ . Under this condition, equation (S6) can be rewritten as

$$\sigma = \frac{A_\sigma}{T} \exp\left(-\frac{E_a}{RT}\right). \quad (\text{S8})$$

with a constant of

$$A_\sigma = \frac{e^2 D_0 n_{\text{Li}}(\phi_{Wt})}{k_B} = \frac{e^2 D_0 n_{\text{Li}}}{k_B}. \quad (\text{S9})$$

As mentioned above, equation (S6) is the Arrhenius expression of ionic conductivity for solid electrolyte.

### **S10.2. $\phi_{Wt} = \phi_{Wt}(T)$ : $\phi_{Wt}$ is a function of temperature**

Yet, if  $\phi_{Wt}$  is a function of temperature:  $\phi_{Wt} = \phi_{Wt}(T)$ , equation (S6) should be written as

$$\sigma = \frac{A_\sigma}{T} \exp\left(-\frac{E_b}{RT}\right). \quad (\text{S10})$$

Here, the influence of temperature-dependent behavior of  $B(\phi_{Wt})$  is embedded in the entropic contribution,  $-T\Delta S$ , on  $E_b$  and  $A_\sigma$  is also a function of temperature as

$$A_\sigma = \frac{e^2 D_0 n_{\text{Li}}(\phi_{Wt}(T))}{k_B}. \quad (\text{S11})$$

## S11. References:

- [R1] Park, J. H.; Jung, S.; Song, Y. H.; Aluru, N. R.; Kim, T.; Lee, S. B.; Choi, U. H.; Lee, J. Water-Assisted Increase of Ionic Conductivity of Lithium Poly(acrylic acid)-Based Aqueous Polymer Electrolyte. *ACS Appl. Energy Mater.* **2020**, 3, 10119-10130.
- [R2] Maurer, J. J.; Eustace, D. J.; Ratcliffe, C. T. Thermal Characterization of Poly(acrylic acid). *Macromolecules* **1987**, 20, 196-202.
- [R3] Rubinstein, M.; Colby, R. H. *Polymer Physics*; Oxford University Press: London, 2003.
- [R4] Ohno, S.; Banik, A.; Dewald, G. F.; Kraft, M. A.; Krauskopf, T.; Minafra, N.; Till, P.; Weiss, M.; Zeier, W. G. Materials Design of Ionic Conductors for Solid State Batteries. *Prog. Energy* **2020**, 2, 022001.
- [R5] Sulatha, M. S.; Natarajan, U. Origin of the Difference in Structural Behavior of Poly(acrylic acid) and Poly(methacrylic acid) in Aqueous Solution Discerned by Explicit-Solvent Explicit-ion MD Simulations. *Ind. Eng. Chem. Res.* **2011**, 50, 11785–11796.
- [R6] Na, Y. W.; Cheon, J. Y.; Kim, J. H.; Jung, Y.; Lee, K.; Park, J. S.; Park, J. Y.; Song, K.S.; Lee, S.B.; Kim, T.; Yang, S. J. All-in-one Flexible Supercapacitor with Ultrastable Performance under Extreme Load, *Sci. Adv.* **2022**, 8, eabl8631.
- [R7] Hess, B.; Kutzner, C.; van der Spoel, D.; Lindahl, E. GROMACS 4: Algorithms for Highly Efficient, Load-Balanced, and Scalable Molecular Simulation. *J. Chem. Theory Comput.* **2008**, 4, 435–447.
- [R8] Berendsen, H. J. C.; Grigera, J. R.; Straatsma, T. P. The Missing Term in Effective Pair Potentials. *J. Phys. Chem.* **1987**, 91, 6269– 6271.
- [R9] Koneshan, S.; Rasaiah, J. C.; Lynden-Bell, R. M.; Lee, S. H. Solvent Structure, Dynamics, and Ion Mobility in Aqueous Solutions at 25 °C. *J. Phys. Chem. B* **1998**, 102, 4193–4204
- [R10] Lee, S. H.; Rasaiah, J. C. Molecular Dynamics Simulation of Ion Mobility. 2. Alkali Metal and Halide Ions Using the SPC/E Model for Water at 25 °C. *J. Phys. Chem.* **1996**, 100, 1420–1425.
- [R11] Dang, L. X. Development of Nonadditive Intermolecular Potentials Using Molecular Dynamics: Solvation of  $\text{Li}^+$  and  $\text{F}^-$  ions in Polarizable Water. *J. Chem. Phys.* **1992**, 96, 6970–6977.
- [R12] Hoover, W. G. Canonical Dynamics: Equilibrium Phase-Space Distributions. *Phys. Rev. A: At., Mol., Opt. Phys.* **1985**, 31, 1695–1697.

- [R13] Nose, S. A. Molecular Dynamics Method for Simulations in the Canonical Ensemble. *Mol. Phys.* **1984**, 52, 255–268.
- [R14] Parrinello, M.; Rahman, A. Crystal Structure and Pair Potentials: A Molecular-Dynamics Study. *Phys. Rev. Lett.* **1980**, 45, 1196–1199.
- [R15] Rahman, A.; Parrinello, M. Polymorphic Transitions in Single Crystals: A New Molecular Dynamics Method. *J. Appl. Phys.* **1981**, 52, 7182–7190.
- [R16] Spěváček, J.; Dybal, J.; Starovoytova, L.; Zhigunov, A.; Sedláková, Z. Temperature-Induced Phase Separation and Hydration in Poly(n-Vinylcaprolactam) Aqueous Solutions: A Study by NMR and IR Spectroscopy, SAXS, and Quantum-Chemical Calculations. *Soft Matter* **2012**, 8, 6110-6119.
- [R17] Willems, T. F.; Rycroft, C. H.; Kazi, M.; Meza, J. C.; Haranczyk, M. Algorithms and Tools for High-Throughput Geometry-Based Analysis of Crystalline Porous Materials, *Microporous Mesoporous Mater.* **2012**, 149, 134-141.
- [R18] Pinheiro, M.; Martin, R. L.; Rycroft, C. H.; Jones, A.; Iglesia, E.; Haranczyk, M. Characterization and Comparison of Pore Landscapes in Crystalline Porous Materials, *J. Mol. Graph. Model.* **2013**, 44, 208-219.
- [R19] Reguera, D.; Rubí, J. M. Kinetic Equations for Diffusion in the Presence of Entropic Barriers. *Phys. Rev. E* **2001**, 64, 061106.
- [R20] Rubí, J. M.; Lervik, A.; Bedeaux, D.; Kjelstrup, S. Entropy Facilitated Active Transport. *J. Chem. Phys.* **2017**, 146, 185101.
- [R21] Goodenough, J. B. Fast Ionic Conduction in Solids. *Proc. R. Soc. Lond. A* **1984**, 393, 215-234.
- [R22] Nuernberg, R. B. Numerical Comparison of Usual Arrhenius-Type Equations for Modeling Ionic Transport in Solids. *Ionics* **2020**, 26, 2405-2412.